1-1-2018

New insights into understanding the exceptional electrochemical performance of P2-type manganese-based layered oxide cathode for sodium ion batteries

Xiaobo Zheng
University of Wollongong, xz963@uowmail.edu.au

Peng Li
University of Wollongong, pl465@uowmail.edu.au

Haojie Zhu
Ningbo University

Kun Rui
University of Wollongong, krui@uow.edu.au

Guoqiang Zhao
University of Wollongong, gz815@uowmail.edu.au

See next page for additional authors

New insights into understanding the exceptional electrochemical performance of P2-type manganese-based layered oxide cathode for sodium ion batteries

Abstract

Sodium ion batteries (SIBs) are emerging as one of the most promising candidates for large-scale energy storage due to the abundance of sodium. Layered manganese-based oxides, owing to relatively high capacity and low cost, exhibit great potential as SIBs cathode materials, but the cycling life remains a big challenge towards practical applications. Herein, unprecedented electrochemical performance is achieved in P2-type layered Na2/3Ni1/3Mn2/3O2 cathode, and new insights into understanding the structure-performance correlation are gained. Na2/3Ni1/3Mn2/3O2 delivers outstanding cycling stability (~ 80% capacity retention for 2000 cycles, 0.01% capacity loss per cycle),excellent rate capability (70.21% capacity retention at 20 C compared to 0.1 C), and a useable reversible capacity of about 84 mAh g-1 through tailoring its operating voltage range of 2.0-4.0 V. Moreover, the crystal structure of Na2/3Ni1/3Mn2/3O2 is investigated in depth at atomic resolution, and sodium atoms located at 2d Wyckoff sites in different layers are clearly observed and directly distinguished for the first time. Both in-situ X-ray diffraction (XRD) and ex-situ high-resolution transmission electron microscopy (HRTEM) results reveal that the exceptional electrochemical performance is mainly attributed to the superior structural stability of Na2/3Ni1/3Mn2/3O2 during the Na+ insertion/extraction process. The present results suggest that P2-type Na2/3Ni1/3Mn2/3O2 is an extremely promising cathode material for advanced long-life SIBs towards grid storage application.

Disciplines

Engineering | Physical Sciences and Mathematics

Publication Details

Zheng, X., Li, P., Zhu, H., Rui, K., Zhao, G., Shu, J., Xu, X., Sun, W. & Dou, S. Xue. (2018). New insights into understanding the exceptional electrochemical performance of P2-type manganese-based layered oxide cathode for sodium ion batteries. Energy Storage Materials, 15 257-265.

Authors

Xiaobo Zheng, Peng Li, Haojie Zhu, Kun Rui, Guoqiang Zhao, Jie Shu, Xun Xu, Wenping Sun, and Shi Xue Dou

New Insights into Understanding the Exceptional Electrochemical Performance of P2-Type Manganese-based Layered Oxide Cathode for Sodium Ion Batteries

Xiaobo Zheng[a], Peng Li[a], Haojie Zhu[b], Kun Rui[a], Guoqiang Zhao[a], Jie Shu[b,*], Xun Xu[a], Wenping Sun[a,*], and Shi Xue Dou[a]

[a]Institute for Superconducting and Electronic Materials, Australia Institute for Innovation Material, University of Wollongong, NSW 2522, Australia

[b]Faculty of Materials Science and Chemical Engineering, Ningbo University, Ningbo 315211, Zhejiang Province, P. R. China

Abstract

Sodium ion batteries (SIBs) are emerging as one of the most promising candidates for large-scale energy storage due to the abundance of sodium. Layered manganese-based oxides, owing to relatively high capacity and low cost, exhibit great potential as SIBs cathode materials, but the cycling life remains a big challenge towards practical applications. Herein, unprecedented electrochemical performance is achieved in P2-type layered $Na_{2/3}Ni_{1/3}Mn_{2/3}O_2$ cathode, and new insights into understanding the structure-performance correlation are gained. $Na_{2/3}Ni_{1/3}Mn_{2/3}O_2$ delivers outstanding cycling stability (~80% capacity retention for 2000 cycles, 0.01% capacity loss per cycle), excellent rate capability (70.21 % capacity retention at 20 C compared to 0.1 C), and a useable reversible capacity of about 84 mAh g^{-1} through tailoring its operating voltage range of 2.0-4.0 V. Moreover, the crystal structure of $Na_{2/3}Ni_{1/3}Mn_{2/3}O_2$ is investigated in depth at atomic resolution, and sodium atoms located at 2d Wyckoff sites in different layers are clearly observed and directly distinguished for the first time. Both in-situ X-ray diffraction (XRD) and ex-situ high-resolution transmission

* Email address: sergio_shu@hotmail.com (J. Shu); wenping@uow.edu.au (W. Sun)

electron microscopy (HRTEM) results reveal that the exceptional electrochemical performance is mainly attributed to the superior structural stability of $Na_{2/3}Ni_{1/3}Mn_{2/3}O_2$ during the Na^+ insertion/extraction process. The present results suggest that P2-type $Na_{2/3}Ni_{1/3}Mn_{2/3}O_2$ is an extremely promising cathode material for advanced long-life SIBs towards grid storage application.

Keywords: manganese-based layered oxide, cut-off voltage, atomic resolution, phase transition, sodium ion batteries

1. Introduction

Owing to increasing demand for energy and serious environmental concerns, cost-effective and sustainable energy storage systems which could smoothly and safely integrate intermittent new energy into the intelligent electric grid are highly required [1,2]. Advances in electrochemical storage system technology are enabling huge changes in new types of facilities, varying from computers, communications, and consumer electronic (3C) products to electric vehicles (EVs) and large-scale stationary energy storage. Notably, high energy and power densities and miniaturization are critically important for 3C products and EVs, whereas for large-scale grid energy storage, relatively low cost and superior calendar life are of greater significance [3].

Sodium ion batteries (SIBs) are surfacing as the most promising alternative to lithium ion batteries in terms of large-scale grid energy storage due to the huge availability of sodium, and are strategically significant for achieving diversity in sustainable and renewable energy storage systems [4-7]. A wide range of cathode materials for SIBs, such as oxides [8-11],

organic compounds [12-14], polyanionic compounds [15-17], and hexacyanoferrates [18-20], have been developed. Manganese-based layered oxides are proposed as potential candidates for high energy and low cost materials for SIBs, which are ideally suited for stationary energy storage. A variety of manganese-based oxides have been developed as SIBs cathodes, such as $Na_{0.67}Mn_{1-x}Mg_xO_2$ [21], $Na_{0.67}Ni_{0.33}Mn_{0.67}O_2$ [22], $Na_{0.66}Li_{0.18}Mn_{0.71}Ni_{0.21}Co_{0.08}O_{2+\delta}$ [23], and $NaNi_{0.5}Mn_{0.4}Ti_{0.1}O_2$ [24]. It should be mentioned that much research attention has been focused on studying their high voltage performance towards high energy density and improving their electrochemical properties through heteroatom doping [22, 25-27]. Although the high voltage performance can be improved to some extent by doping, the long-term cycling stability, which is closely associated with the structural stability of the cathodes during the Na^+ insertion/extraction process, is still a daunting scientific challenge. On the other hand, SIBs are intended to be applied in grid-scale energy storage (targeting intermittent renewable energy sources) where energy density is not the first consideration compared to cost, safety, and cyclability. Therefore, tailoring operating voltage ranges of the cathode materials to avoid undesired phase transformation and to eventually achieve good cycling stability is of great significance. Although there have some reports discussing the electrochemical performance of manganese-based cathodes at different operating voltage ranges, these studies are not sufficiently systematical and in-depth in terms of unraveling the voltage-performance-structure relationship [28, 29].

Herein, the electrochemical performance of $Na_{2/3}Ni_{1/3}Mn_{2/3}O_2$ in different operating voltage ranges was systematically investigated, and specific attention was focused on the

ultra-long-term performance stability. The surprisingly durable performance along with excellent rate capability were achieved for the cell in the operating voltage range of 2.0-4.0 V, with 80% capacity retention after 2000 cycles and with 70.2 % capacity retention at 20 C compared to 0.1 C. In-situ XRD and HRTEM were conducted to unravel the structure-performance correlation of the cathode during the Na^+ insertion/extraction process, and revealed that the crystal structure stability of the electrode is the origin for the exceptional electrochemical performance.

2. Experimental section

2.1 Material Synthesis

P2-type $Na_{2/3}Ni_{1/3}Mn_{2/3}O_2$ (SNMO) powders were synthesized through a typical solid-state reaction from stoichiometric amounts of Na_2CO_3 (Sigma-Aldrich, 99.95%), NiO (Sigma-Aldrich, 99.8%), and Mn_2O_3 (Sigma-Aldrich, 99%). The mixtures were ground using a mortar and pestle, and then stirred in ethanol solution in a beaker for 2 h. The obtained powders were dried at 80˚C overnight and then calcined at 920 ˚C in compressed air for 12 h. In order to avoid contamination by moisture, the as-prepared powders were stored in a glove box filled with Ar.

2.2 Materials Characterization:

The phase structure of the obtained SNMO powders was characterized by X-ray diffraction (XRD) (GBC MMA diffractometer, λ = 1.541 Å, step size of $0.02^o s^{-1}$). X-ray Rietveld refinement was conducted and analyzed by GSAS software [30], and the data was collected in the 2θ range of 10^o-80^o, with the scan rate of $0.5^o \cdot min^{-1}$. A homemade cell

equipped with an X-ray-transparent beryllium window was applied for *In-situ* XRD tests, which were collected using a Bruker AXS D8 Focus powder X-ray Diffractometer with a $Cu_{k\alpha}$ radiation (λ=1.541 Å) [31]. The *In-situ* XRD patterns were scanned for each 2θ from 10 ^{o} to 60^{o}, between 2.0-4.0 V and 2.0-4.3 V.

The morphologies of the SNMO powders and the SNMO electrodes were investigated by field-emission scanning electron microscopy (FESEM, JEOL JSM-7500) and transmission electron microscopy (TEM, JEM-2010). Annular bright field (ABF) and high-angle annular dark field (HAADF) images were conducted on a 200 kV ARM-200F transmission electron microscope (JEOL) with a double aberration corrector and a cold field-emission gun.

2.3 Electrochemical measurements:

The electrode slurry was prepared by thoroughly mixing the SNMO powders (80 wt.%), Super P (10 wt.%), and polyvinylidene fluoride (10 wt.%), in N-methyl pyrrolidinone (NMP) using mortar and pestle. The slurry was coated on the aluminum foil by using a doctor blade and then dried at 120 ^{o}C for 12 h in a vacuum oven. The CR2032 coin-type cells were assembled in an Ar-filled glove box with both H_2O and O_2 levels less than 1 ppm. Metallic sodium foil was used as the counter/reference electrode, and glass fiber paper was used as the separator. 1 M $NaClO_4$ (1 M) dissolved in a mixture of ethylene carbonate and propylene carbonate with a volume ratio of 1:1 was employed as the electrolyte. The galvanostatic charge/discharge testing was conducted on a NEWARE battery test system at room temperature. Two operating voltage ranges, 2.0-4.0 V and 2.0-4.3 V, were studied. Cyclic voltammetry tests were carried out at a scan rate of 0.1 mV s^{-1} in the voltage windows of

2.0-4.0 V and 2.0-4.3 V. Electrochemical impedance spectroscopy (EIS) tests were performed using Bio-Logic potentiostat in a frequency range of 1 MHz–10 mHz with an AC amplitude of 10 mV. The galvanostatic intermittent titration technique was adopted to analyze the evolution of the sodium ion diffusion coefficient during Na^+ insertion/extraction, which was carried out on a Land battery testing system. All the cells were firstly cycled at 0.1 C for 4 cycles to reach their equilibrium state. Subsequently, the cells were charged at 0.1 C for 10 min, and then rested for 60 min to achieve a nearly equilibrium state, and the cells were charged for 10 min again until to cut-off voltage.

3. Results and discussion

Figure 1a shows the Rietveld refinement of the X-ray diffraction (XRD) pattern of SNMO, where all the diffraction peaks correspond well to a hexagonal lattice with the $P6_3/mmc$ space group, indicating that no secondary phases or impurities are detectable. The Rietveld refinement results are displayed in Table S1, where the lattice parameters *a* and *c* are 2.8850(7) Å and 11.1663(5) Å, respectively. The good refinement results can be verified by the low weighted profile and profile R-factors, R_{wp} and R_p, which are reliability indices demonstrating that pure and highly crystalline SNMO was synthesized successfully.

A schematic diagram of crystal structure of layered SNMO is displayed in **Figure 1**b, which is a typical hexagonal close packed (hcp) crystal with ABBA stacking of oxygen layers. As shown in Table S1, transition metal elements are accommodated at the 2a Wyckoff sites, but Na^+ occupies two different prismatic sites, with the Na_f (2b Wyckoff sites) and Na_e (2d Wyckoff sites) positions, respectively. The Na^+ ions located at 2b sites coordinate with 6

oxygen ions to form trigonal prisms, which share two faces (top and bottom) with MO_6 (M = Ni and Mn) octahedra. In contrast, the Na ion accommodated at 2d positions (Na_e) has trigonal prismatic oxygen coordination similar to Na^+ ions with 2b position but sharing with six edges with transition metal octahedral (MO_6), which is indicated in **Figure 1**b. The morphology of the obtained SNMO was investigated by scanning electron microscopy (SEM), as shown in Figure S1 in the Supporting Information. It was found to have plate shaped particles with a relatively uniform particle size of 500 nm - 3 μm. The inset indicated in **Figure 1**a is the high resolution SEM image of SNMO, demonstrating that the primary particles of SNMO have a typical layered shape, which can usually be found in insertion materials.

In order to better understand the crystal structure of SNMO at atomic resolution, high-angle annular dark field (HAADF) and annular bright field (ABF) scanning transmission electron microscopy (STEM) techniques were employed. The atomic positions of the transition metals (Ni and Mn) and sodium were revealed by the blue bright-dot contrast in the HAADF-STEM image (**Figure 2**a) and the dark-dot contrast in the ABF-STEM image (**Figure 2**b). The observation direction is along [001] and sodium atoms with the 2b Wyckoff sites (Na_f) are in the same column with transition metal atoms, hence it appears that one sodium atom (transition metal atom) is coordinated by six transition atoms in plane, as shown in the schematic illustration of SNMO (**Figure 2**c) viewed along the *c*-axis. However, unraveling the distribution situation of two different site sodium atoms is of great significance, which is vital to better understanding of the local environmental of sodium and

transition metal atoms. Inverse Fast Fourier Transformation (IFFT) technique, therefore, was applied. **Figure 2**d derived from **Figure 2**a through IFFT techniques clearly indicates the distribution of sodium atoms projected from [001] direction, in which sodium atoms (Na_e) with different layers were obviously observed and distinguished. To more vividly demonstrate it, colored image of **Figure 2**d is displayed in **Figure 2**e, where transition atoms and sodium atoms with different layers can be observed more clearly, and it can be observed that one transition metal atom is surrounded by six Na_e atoms. In order to better differentiate them, the Nae atoms located in upper layer and bottom layer are denoted as Nae1 with yellow color and Nae2 with purple color, respectively. **Figure 2**f is the schematic illustration of the crystal structure of P2-SNMO material from different directions, which is highly congruent with the results observed from IFFT images. To the best of our knowledge, moreover, it has to be mentioned that it is the first time that sodium atoms (Na_e) located at different layers are clearly observed and directly distinguished. The Fast Fourier Transformation (FFT) pattern of SNMO projected along the [001] axis is indicated in **Figure 2**g, where typical hexagonal crystal system was observed, and the crystal planes can be indexed to the corresponding reflections derived from the P2-type layered structure, which is identical to what was found from the XRD Rietveld refinement and can be further verified by Figure S2. STEM mapping was conducted to identify the distribution of elements (**Figure 2**h and **2**i), which clearly indicates that nickel, manganese, sodium, and oxygen elements are extremely uniform in the material. This is also confirmed by the corresponding element concentration spectra (Figure S3), in which the concentrations of all the elements remain nearly constant in the bulk and are

gradually reduced in the edges of the bulk, revealing that the elements are distributed homogeneously in the material.

The electrochemical performance of SNMO electrode in different voltage ranges was evaluated and the performance profiles are illustrated in **Figure 3**. In the first charging-discharging curves (**Figure 3**a), several charge and discharge plateaus are observed below 4 V, which are either single-phase or two-phase regions with similar lattice constants, related to Na^+ / vacancy ordering occurring within the sodium layer. However, the electrode charged to 4.3 V (SNMO-4.3) shows a long platform at around 4.2 V, which is ascribed to the phase transformation from P2 to O2, accompanied by the gliding and expansion of transition-metal layers [32, 33]. The schematic illustration of phase transition process of SNMO is showed in Figure S4. The SNMO samples deliver discharge capacity of 84 and 123 mAh g^{-1} at 4.0 and 4.3 V at 0.05 C (1 C = 170 mAh g^{-1}), respectively. Although SNMO-4.3 delivers more than a third as much capacity as SNMO-4.0, the specific capacity of SNMO-4.3 fades rapidly compared to SNMO-4.0, as shown in **Figure 3b**. There is negligible reversible capacity fading (with 97.2% capacity retention at 1 C) after 100 cycles for SNMO-4.0; however, only 59.93 % capacity retention is maintained for SNMO-4.3. The inferior cycling performance of SNMO-4.3 is in great part due to the irreversible phase transition [22, 32]. When the voltage reaches 4.3 V, most sodium ions are extracted from the host structure, and this is beneficial for the formation of O2 phase because it is more energetically stable when the host structure contains few sodium ions [32, 33]. Owing to the phase transition, significant volume change would occur correspondingly, which would

deteriorate the bonding between the electrode and the current collector, as shown in Figure S5, resulting in deteriorated current collecting ability of the electrode. The SEM images of the electrodes operating at different voltage ranges and cycles (Figure S6 and Figure S7, Supporting Information) provide more details regarding the morphology change of the electrode. For SNMO-4.0, no obvious changes could be observed before and after 2000 cycles in terms of the morphology or the particle size of the active material, as well as the uniform distribution of the conductive additive (Super P). In contrast, the SNMO-4.3 electrode morphology changes greatly over cycling. The conductive additive particles appear to be seriously agglomerated and separated from the active materials, eventually resulting in seriously degraded electronic conduction behavior and hence capacity fading accordingly. The way of electronic conduction is also transferred from oxide-carbon-oxide phase boundaries to oxide-oxide grain boundaries when increasing the cut-off voltage from 4.0 to 4.3 V, and this process is schematically illustrated in Figure S8. More seriously, it seems that the stacking faults of O2 phase is not fully eliminated in the discharge process, resulting in dramatic capacity decay during following cycles [28]. Clearly, the plateau at around 4.2 V disappears gradually over cycling (Figure S9, Supporting Information), which is closely accompanied by the dramatic capacity fading at high voltage. The extremely high cycling stability of SNMO-4.0 can be attributed to the stable phase structure during charge/discharge process. **Figure 3**c presents the rate performance of SNMO-4.0 and SNMO-4.3. After cycled 5 times at 0.1 C and 0.5 C, respectively, SNMO-4.0 delivers a reversible capacity of 75.6 mAh g^{-1} at 1 C (88.9% retention as compared with 0.1 C), and a surprisingly high capacity

retention of 70.21% is reached at a high rate of 20 C (3400 mA/g). In contrast, SNMO-4.3 displays inferior rate performance, and nearly no capacity can be delivered at 5 C. The sluggish electronic contact and obstructed Na^+ transport induced by phase transition as discussed previously should be responsible for the huge rate performance difference. Inspired by the remarkable cycling stability and the superior rate capability of SNMO-4.0, cycling performance at a high rate of 10 C (1700 mA/g) was tested as plotted in **Figure 3**d. Impressively, SNMO-4.0 still delivers ultra-stable capacity at 10 C, with an average capacity loss of about 0.072% per cycle and a high Coulombic efficiency of 99%. An ultra-long calendar life is absolutely essential for batteries towards grid storage application, which in turn helps to reduce system cost. Therefore, super-long cycling (2000 cycles) of SNMO-4.0 was conducted at 1 C at room temperature. As shown in **Figure 3**e, SNMO-4.0 exhibits exceptionally cycling performance. 80% capacity retention is maintained after 2000 cycles, with the capacity loss rate of only about 0.01% per cycle. Moreover, the average Coulombic efficiency reaches 99.7%, corroborating the excellent cycling stability. It has to be noted that SNMO-4.0 delivers one of the best electrochemical performances, to the best of our knowledge, among all of the manganese-based layered materials for SIBs [34-37]. The exceptional cycling and rate performance of SNMO-4.0 may enable SIBs to partly substitute for lithium ion batteries and be widely applied in large-scale energy storage devices.

In situ XRD of both electrodes were conducted to unravel the nature of these discrepancies. The changes in the diffraction peak position with the time are indicated in **Figure 4**, mainly for the (002), (004), (100) and (012) reflections. The overall structural

evolution of SNMO demonstrates that a solid-solution reaction occurs when the cell is charged to 4.0 V. However, when the electrode crosses the long plateau around 4.2 V, a new peak, assigned to (002′), which is sited at about 21°, emerges upon Na ion extraction, confirming that a phase transition occurs from P2 to O2 and the electrode is in a two-phase, coexistence state (**Figure 4** h and **4**j). As indicated in Figure S10, a phenomenon of anisotropic evolution of the lattice parameters was observed, where *a* lattice parameter decreases gradually and then is maintained after 1/3 Na^+ extracted from host structure during charge process. However, the *c* lattice parameter increases slightly and then decrease intensively when phase transformation occurs, where less than 1/3 Na^+ remains. Also, the lattice volume decreases slightly when 1/3 Na^+ extracted from the structure and after that a drastic decrease occurs due to the formation of O2 phase. This phenomenon also can be demonstrated by the concurrent shift to lower angles for the (00*l*) reflections (such as (002) and (004)), but a shift to higher angle for (*hk0*) reflections (such as 100) during charge process, or vice versa. The *in situ* XRD results indicate that SNMO-4.0 electrode maintains good structural stability and high reversibility upon Na^+ insertion/extraction, thereby yielding superior cycle performance.

To discover the reasons for the huge difference in electrochemical performance between SNMO-4.0 and SNMO-4.3, the sodium ion diffusion coefficient (D_{Na+}) was determined by the galvanostatic intermittent titration technique (GITT). The D_{Na}+ can be obtained from the following formula:

$$D_{\mathrm{Na^+}} = \frac{4}{\pi}\left(\frac{m_B V_m}{M_B S}\right)^2 \left(\frac{\Delta E_s}{\tau\left(\frac{dE_\tau}{d\sqrt{\tau}}\right)}\right)^2 \left(\tau \ll \frac{L^2}{D_{Li^+}}\right) \quad (1)$$

Where τ is the constant current pulse time, S represents the contact area between the electrode and electrolyte (here, the geometric surface of the SNMO electrode), while m_B , V_m, and M_B are the actual mass, the molar volume, and the molar mass of the SNMO materials, respectively. ΔE_s is the voltage difference from the steady-state voltage during a single-step GITT process. **Figure 5**a presents typical GITT profiles of the SNMO electrodes during the entire charging process, and a single-step procedure is indicated in **Figure 5**b. As indicated in **Figure 5**c, the cell voltage as a function of $\tau^{1/2}$ shows a linear relationship, and therefore, Eq. (1) could be rewritten as Eq. (2):

$$D_{Na^+} = \frac{4}{\pi}\left(\frac{m_B V_m}{M_B S}\right)^2 \left(\frac{\Delta E_s}{\Delta E_\tau}\right)^2 \left(\tau \ll \frac{L^2}{D_{Li^+}}\right) \quad (2)$$

$D_{\mathrm{Na+}}$, as a function of cell potential for the SNMO electrode, which is obtained from titration curves and this equation, is presented in **Figure 5**d. Between the voltages of 2.2 V and 3.8 V, the diffusion coefficient is 1.8 (± 0.6) $\times 10^{-10}$ $\mathrm{cm^2/s}$, which is regarded as a relatively fast diffusion process for layered-structure cathode materials for SIBs [41]. The structural rearrangement or exhaustion of certain processes may lead to minima of the diffusion coefficient, which could exist because the structural transformation yields different diffusion pathways for $\mathrm{Na^+}$ insertion/extraction. Two small minima are displayed in this voltage range, corresponding well to the redox peaks in the CV curves and the plateaus at around 3.40 and 3.65 V in the charging profile, which indicates that there are $\mathrm{Na^+}$/vacancy ordering processes between the $\mathrm{MO_2}$ slabs [39]. An obvious minimum is located at around 4.2 V, which can be

ascribed to the phase transition from P2 to O2. GITT test indicates that the phase transition occurs at a potential lower than that was observed from CV and charge/discharge profiles. This deviation can be likely attributed to the inherent nature of the GITT method, which has also been previously reported [38, 40]. Thereafter, D_{Na^+} decreases monotonically from 10^{-11} to 10^{-12} and finally 10^{-14} cm^2/s at the end of charging, which is usually observed in O2 phase layered materials [41]. The severely decreased D_{Na^+} should be responsible for the poor rate performance of SNMO-4.3.

CV tests were performed to further explore the desodiation and sodiation mechanisms of SNMO in the different voltage ranges, as shown in **Figure 6**. During the first cycle, the main redox couples observed can be assigned to the nickel redox process, but when the electrode is charged to 4.3 V, there is an additional redox couple located at 4.2/4.05 V, corresponding to the phase transformation from prismatic P2-type to octahedral O2-type. For SNMO-4.0, negligible peak shifts can be observed with prolonged cycling, even after 1000 cycles at 1 C, indicating the superior structural stability and the surprisingly high reversibility of the desodiation and sodiation reaction, which is in good agreement with the dQ/dV curves indicated in Figure S11. Nevertheless, CV curve of SNMO-4.3 exhibits significant difference in terms of peak position and current density after cycling. For instance, the redox peak located at 4.2/4.05 V almost disappears after 100 cycles, which is consistent with the disappearance of the plateau at 4.2 V (Figure S11) [32]. Also, the polarization tends to become severe with prolonged cycling for SNMO-4.3. There is no doubt that the CV results confirm the cycling superiority of SNMO-4.0.

Electrochemical impedance spectroscopy (EIS) was carried out to further analyze the electrochemical properties of the SNMO samples. Nyquist plots and the typical equivalent circuit are presented in Figure S12. As shown in Figure S12 and Table S2, both the R_{sf} and the R_{ct} values of SNMO-4.0 and SNMO-4.3 increase with cycling, but R_{ct} rises more significantly. SNMO-4.0 (80.6 Ω) shows much smaller R_{ct} than that of SNMO-4.3 (2529.0 Ω), suggesting faster charge transfer kinetics of SNMO-4.0. It can be clearly seen that R_{ct} of SNMO-4.3 increases much more dramatically than SNMO-4.0 over cycling. R_{ct} of SNMO-4.3 rises to 11658.0 Ω after 103 cycles, while R_{ct} of SNMO-4.0 is only 581.4 Ω even after 1003 cycles. The EIS results also provide solid evidence to prove the excellent cycling and rate performance of SNMO-4.0.

To further elucidate the crystal structure stability of the SNMO-4.0 electrode, *ex-situ* XRD and HRTEM after 2000 cycles at 1 C were also carried out. The XRD patterns of the pristine SNMO powder (red line) and SNMO-4.0 electrode after 2000 cycles at 1 C (blue line) are displayed in **Figure 7**a. It can be seen that no obvious changes or extra peaks (except for the peak of Al foil) can be observed between the pristine sample and the electrode after 2000 cycles, both of which correspond well to the P2-type layered structure (space group P63/mmc), demonstrating that the structure of SNMO is well maintained even after such tough cycling. To make this point clear, XRD Rietveld refinement was conducted and the results are presented in **Figure 7**e and Table S3. It can be seen that the lattice parameters (a=b=2.898(2), c=11.184(3)) only exhibit minor changes compared to pristine sample, and accordingly the cell volume expands a little bit (V=81.360 Å^3), near 0.001% average volume

expansion per cycle), implying very appealing structural reversibility and stability upon charge/discharge process. The exceptional crystal structure stability over 2000 cycles is also confirmed by HRTEM results. As can be seen from **Figure 7**b, the lattice spacing of 0.559 nm can be indexed to (002) crystal plane of P2-type SNMO. The SAED patterns along the [010] and [001] axis further confirms that the typical hexagonal structure of P2-type SNMO.

4. Conclusions

In summary, we, for the first time, demonstrated ultra-stable cycling performance (2000 cycles) along with exceptional rate capability in P2-type manganese-based layered oxide cathodes for SIBs. P2-type $Na_{0.67}Ni_{0.33}Mn_{0.67}O_2$ was selected as a model cathode and investigated in detail in terms of performance-structure relationship. The crystal structure of $Na_{0.67}Ni_{0.33}Mn_{0.67}O_2$ was analyzed in depth by utilizing STEM techniques, and sodium atoms (Na_e) located at different layers were clearly observed and directly distinguished for the first time. The in-situ XRD, ex-situ HRTEM and SEM results indicate that the crystal structure transformation and the consequent changes in the pathways for electronic conduction upon Na^+ insertion/extraction are considered as the major reason for the significant electrochemical performance difference between 4.0 and 4.3 V voltage cut-offs. Surprisingly excellent cycling stability (80% capacity retention after 2000 cycles) and remarkable rate performance (70.2 % capacity retention at 20 C compared to 0.1 C) were achieved for the SNMO-4.0 electrode due to superior structural stability. Such exciting findings provide solid evidence to prove that $Na_{0.67}Ni_{0.33}Mn_{0.67}O_2$ shows great potential as the SIBs cathode for grid storage application, and also shed light on developing new robust layered oxide-based cathodes.

Acknowledgements

This work was financially supported by Australian Research Council (ARC) DECRA Grant (DE160100596) and Linkage Project (LP160100273). X. B. Zheng is supported by the China Scholarship Council (No. 201606370044). The authors would like to thank Dr. Tania Silver for critical reading of this paper and Dr. David Mitchell for STEM technique support.

Conflict of interest

The authors declare no competing financial interest.

References

[1] B. Dunn, H. Kamath and J.-M. Tarascon, Science 334 (2011) 928-935.
[2] J.-Y. Hwang, S.-T. Myung and Y.-K. Sun, Chem. Soc. Rev. 46 (2017) 3529-3614.
[3] D. Kundu, E. Talaie, V. Duffort and L. F. Nazar, Angew. Chem. Int. Ed. 54 (2015) 3431-3448.
[4] N. Yabuuchi, K. Kubota, M. Dahbi and S. Komaba, Chem. Rev. 114 (2014) 11636-11682.
[5] Y. Wang, R. Xiao, Y.-S. Hu, M. Avdeev and L. Chen, Nat Commun 6 (2015) 6954.
[6] M. H. Han, E. Gonzalo, G. Singh and T. Rojo, Energy Environ. Sci. 8 (2015) 81-102.
[7] N. Ortiz-Vitoriano, N. E. Drewett, E. Gonzalo and T. Rojo, Energy Environ. Sci. 10 (2017) 1051-1074.
[8] J. Y. Hwang, S. M. Oh, S. T. Myung, K. Y. Chung, I. Belharouak and Y. K. Sun, Nat Commun 6 (2015) 6865.
[9] N. Yabuuchi, M. Kajiyama, J. Iwatate, H. Nishikawa, S. Hitomi, R. Okuyama, R. Usui, Y. Yamada and S. Komaba, Nat. Mater. 11 (2012) 512.
[10] B. Zhang, R. Dugas, G. Rousse, P. Rozier, A. M. Abakumov and J.-M. Tarascon, Nat Commun 7 (2016) 10308.
[11] N. Sharma, E. Gonzalo, J. C. Pramudita, M. H. Han, H. E. Brand, J. N. Hart, W. K. Pang, Z. Guo and T. Rojo, Adv. Funct. Mater. 25 (2015) 4994-5005.
[12] W. Luo, M. Allen, V. Raju and X. Ji, Adv. Energy Mater. 4 (2014) 1400554.
[13] K. Sakaushi, E. Hosono, G. Nickerl, T. Gemming, H. Zhou, S. Kaskel and J. Eckert, Nat Commun 4 (2013) 1485.
[14] S. Wang, L. Wang, Z. Zhu, Z. Hu, Q. Zhao and J. Chen, Angew. Chem. Int. Ed. 126 (2014) 6002-6006.
[15] M. Chen, L. Chen, Z. Hu, Q. Liu, B. Zhang, Y. Hu, Q. Gu, J. L. Wang, L. Z. Wang and X. Guo, Adv. Mater 29 (2017) 6670.
[16] X. Rui, W. Sun, C. Wu, Y. Yu and Q. Yan, Adv. Mater 27 (2015) 6670-6676.

[17] Q. Zhang, W. Wang, Y. Wang, P. Feng, K. Wang, S. Cheng and K. Jiang, Nano Energy 20 (2016) 11-19.
[18] Y. Jiang, S. Yu, B. Wang, Y. Li, W. Sun, Y. Lu, M. Yan, B. Song and S. Dou, Adv. Funct. Mater. 26 (2016) 5315-5321.
[19] L. Wang, Y. Lu, J. Liu, M. Xu, J. Cheng, D. Zhang and J. B. Goodenough, Angew. Chem. Int. Ed. 52 (2013) 1964-1967.
[20] Y. You, X.-L. Wu, Y.-X. Yin and Y.-G. Guo, Energy Environ. Sci. 7 (2014) 1643-1647.
[21] J. Billaud, G. Singh, A. R. Armstrong, E. Gonzalo, V. Roddatis, M. Armand, T. Rojo and P. G. Bruce, Energy Environ. Sci. 7 (2014) 1387-1391.
[22] P. F. Wang, Y. You, Y. X. Yin, Y. S. Wang, L. J. Wan, L. Gu and Y. G. Guo, Angew. Chem. Int. Ed. 55 (2016) 7445-7449.
[23] S. Guo, P. Liu, H. Yu, Y. Zhu, M. Chen, M. Ishida and H. Zhou, Angew. Chem. Int. Ed. 54 (2015) 5894-5899.
[24] H.-R. Yao, P.-F. Wang, Y. Gong, J. Zhang, X. Yu, L. Gu, C. OuYang, Y.-X. Yin, E. Hu and X.-Q. Yang, J. Am. Chem. Soc. 139 (2017) 8440-8443.
[25] E. Talaie, V. Duffort, H. L. Smith, B. Fultz and L. F. Nazar, Energy Environ. Sci. 8 (2015) 2512-2523.
[26] E. de la Llave, E. Talaie, E. Levi, P. K. Nayak, M. Dixit, P. T. Rao, P. Hartmann, F. Chesneau, D. T. Major and M. Greenstein, Chem. Mater. 28 (2016) 9064-9076.
[27] J. Xu, D. H. Lee, R. l. J. Clément, X. Yu, M. Leskes, A. J. Pell, G. Pintacuda, X.-Q. Yang, C. P. Grey and Y. S. Meng, Chem. Mater. 26 (2014) 1260-1269.
[28] H. Wang, B. Yang, X.-Z. Liao, J. Xu, D. Yang, Y.-S. He and Z.-F. Ma, Electrochim. Acta. 113 (2013) 200-204.
[29] S. Komaba, N. Yabuuchi, T. Nakayama, A. Ogata, T. Ishikawa and I. Nakai, Inorg Chem 51 (2012) 6211-6220.
[30] B. H. Toby, J. Appl. Crystallogr. 34 (2001) 210-213.
[31] J. Shu, M. Shui, D. Xu, Y. Ren, D. Wang, Q. Wang, R. Ma, W. Zheng, S. Gao and L. Hou, J. Mater. Chem. 22 (2012) 3035-3043.
[32] Z. Lu and J. Dahn, J. Electrochem. Soc.148 (2001) A1225-A1229.
[33] D. H. Lee, J. Xu and Y. S. Meng, Phys. Chem. Chem. Phys. 15 (2013) 3304-3312.
[34] P.-F. Wang, Y. You, Y.-X. Yin and Y.-G. Guo, Adv. Energy Mater. 2017 1701912.
[35] P.-F. Wang, H-R Yao, X-Y Liu,J-N Zhang, L Gu, X-Q Yu, Y.-X. Yin and Y.-G. Guo, Adv. Mater. 29 (2017) 1700210.
[36] P.-F. Wang, H-R Yao, X-Y Liu, Y.-X. Yin, J-N Zhang,Y.R. Wen,X.Q Yu, L Gu and Y.-G. Guo. Sci. Adv., 2018, 4, eaar6018.
[37] P.-F. Wang, Y-J Guo, H. Duan, T-T Zuo, E. Y. Hu, K. Attenkofer, H. L. Li, X. S. Zhao, Y-X Yin, X.Q. Yu and Y.-G. Guo. ACS Energy Lett. 2 (2017) 2715-2722
[38] N. Bucher, S. Hartung, J. B. Franklin, A. M. Wise, L. Y. Lim, H.-Y. Chen, J. N. Weker, M. F. Toney and M. Srinivasan, Chem. Mater. 28 (2016) 2041-2051.
[39] K. Shaju, G. S. Rao and B. Chowdari, Electrochim. Acta. 49 (2004) 1565-1576.
[40] E. Markevich, M. Levi and D. Aurbach, J. Electroanal. Chem. 580 (2005) 231-237.

[41] K. Shaju, G. S. Rao and B. Chowdari, Electrochim. Acta. 48 (2003) 2691-2703.

Figure captions

Figure 1 (a) XRD Rietveld refinement of SNMO material. The insert is SEM image of the as-prepared SNMO material. (b) Schematic illustration of the crystal structure of SNMO material, A and B stand for two different stacking arrangements of oxygen layers.

Figure 2 (a) HAADF-STEM image of SNMO. (b) ABF-STEM image of SNMO. (c) Schematic illustration of SNMO crystal viewed along the [001] zone axis. (d) IFFT image of HADDF-STEM image. (e) Colored IFFT image. (f) Schematic illustration of SNMO showed the sodium atoms with different Wyckoff sites at different layers. (g) FFT pattern of SNMO viewed from [001] direction (h) STEM image of SNMO sample. (i) STEM chemical mapping for Na, Ni, Mn and O.

Figure 3 Electrochemical performance of P2-SNMO in different voltage ranges. (a) Typical initial charge-discharge curves. (b) Cycling performance at 1 C. (c) Rate performance. (d) Cycling performance of SNMO-4.0 at a high rate (10 C). (e) Ultra-long cycling performance of P2-SNMO-4.0 at 1 C rate over 2000 cycles.

Figure 4 Structural evolution of SNMO-4.0 samples during Na^+ insertion/extraction process. (a) and (b) *In situ* XRD patterns collected at first and second cycles. Selected 2θ ranges of *In situ* XRD patterns indicating the evolution of the (c) 002, (d) 004, (e) 100, and (f) 012 reflections. Structural evolution of SNMO-4.3 samples during Na^+ insertion/extraction process. (g) and (h) *In situ* XRD patterns of SNMO-4.3 electrode. Selected 2θ ranges of *In situ* XRD patterns showing the evolution of the (i) 002, (j) 004, (k) 100, and (l) 012 reflections.

Figure 5 (a) GITT profiles for charge of SNMO electrode in the voltage window of 2.8-4.3 V. (b) Current vs. cell potential for a single titration step in GITT. (c) Linear fit of the cell potential vs. the square root of time ($\tau^{1/2}$) with different pulse currents. (d) Diffusion coefficient of Na^+ vs. cell voltage.

Figure 6 (a) The CV profiles of SNMO-4.0 electrode at different cycles. (b) CV curves of SNMO-4.3 electrode at different cycles.

Figure 7 (a) XRD pattern of SNMO-4.0 after 2000 cycles at 1 C rate. (b) HRTEM image of SNMO-4.0 electrode after 2000 cycles. SAED patterns viewed from the [001] (c) and [110] (d) directions. (e) XRD Rietveld refinement of SNMO-4.0 after 2000 cycles at 1 C rate.

Figure 1

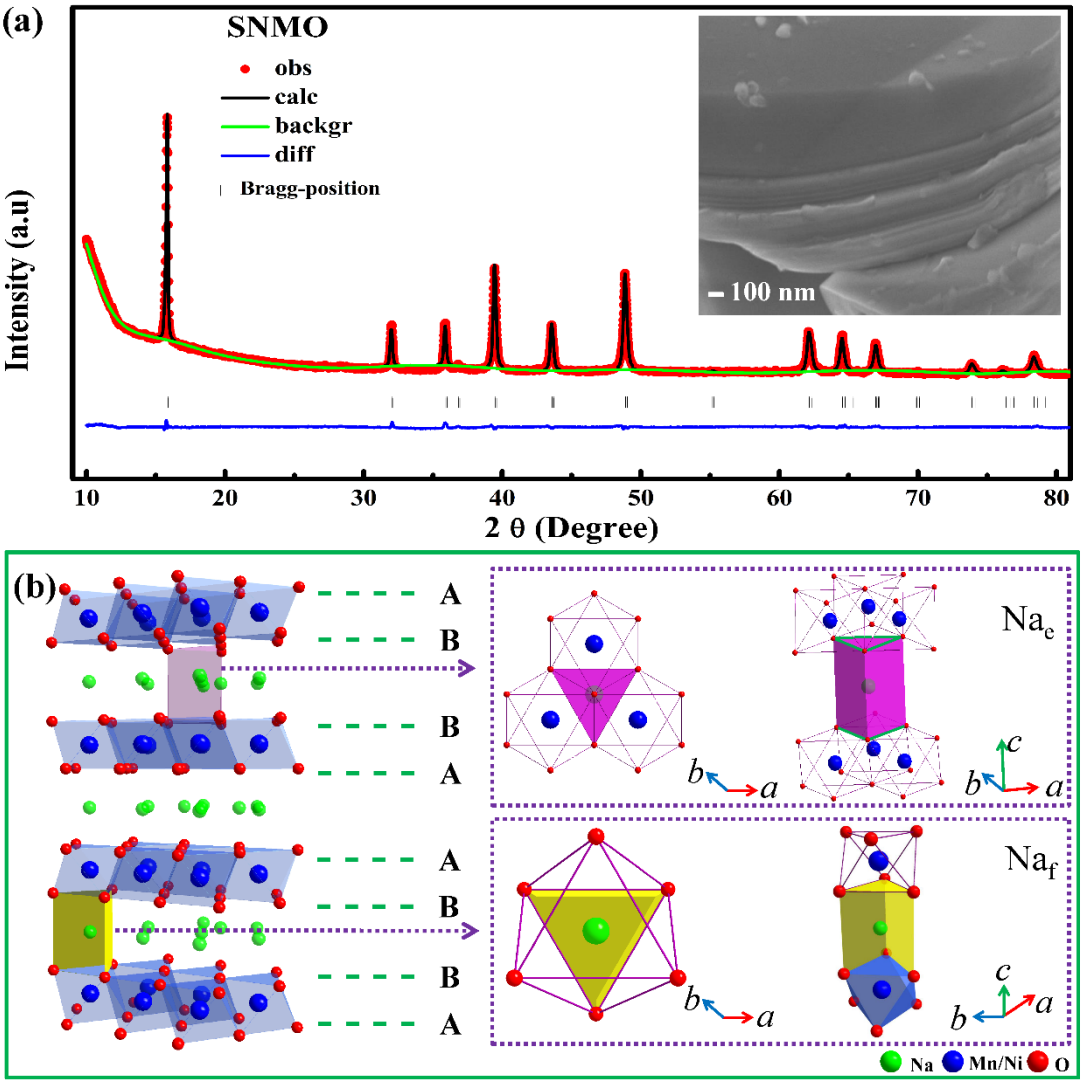
(a)
SNMO
obs
calc
backgr
diff
Bragg-position
Intensity (a.u)
100 nm
10
20
30
40
50
60
70
80
2 θ (Degree)
(b)
A
B
B
A
A
B
B
A
Na$_e$
Na$_f$
b
a
c
Na
Mn/Ni
O

Figure 2

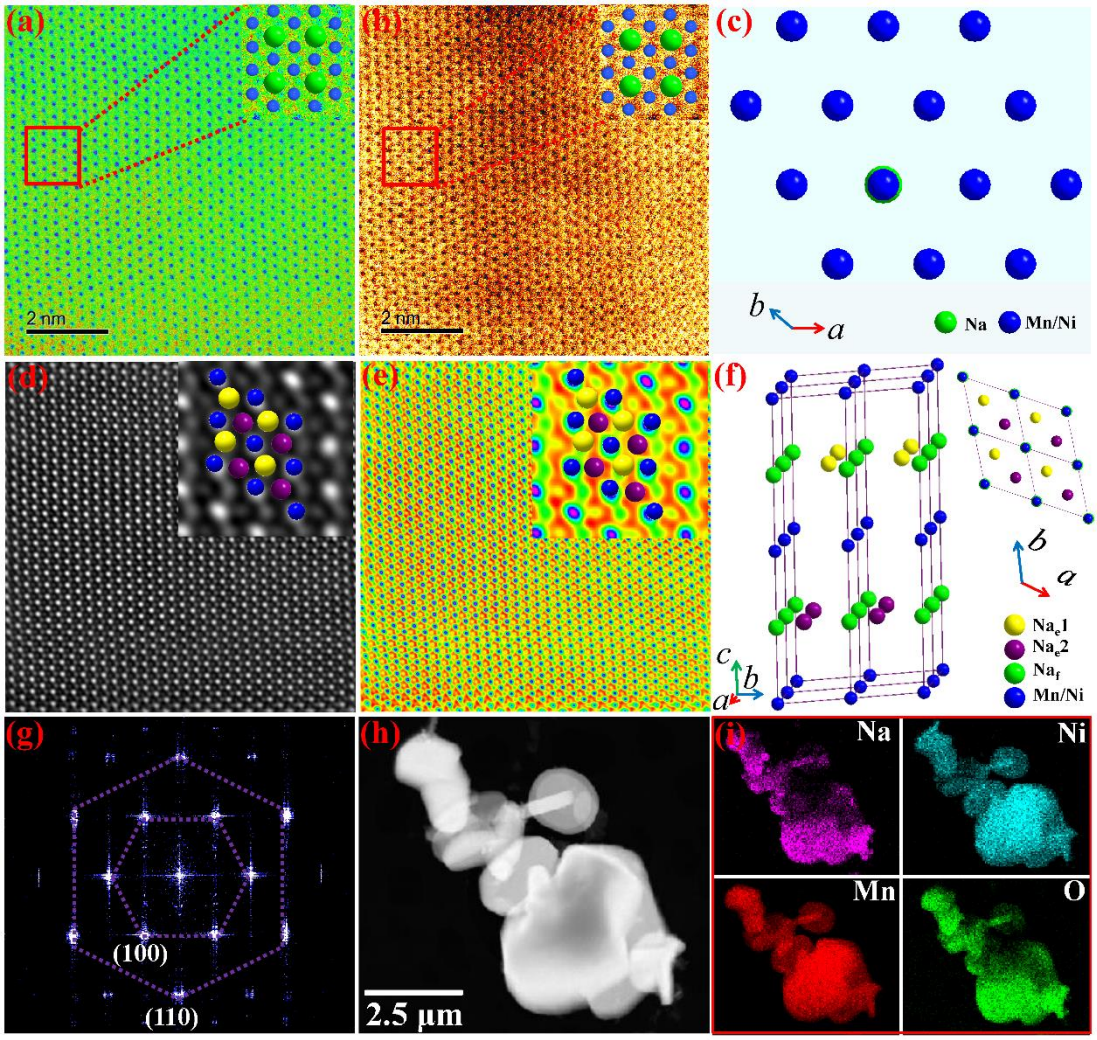
(a)
2 nm
(b)
2 nm
(c)
b
a
Na
Mn/Ni
(d)
(e)
(f)
b
a
c
b
a
Na$_e$1
Na$_e$2
Na$_f$
Mn/Ni
(g)
(100)
(110)
(h)
2.5 μm
(i)
Na
Ni
Mn
O

Figure 3

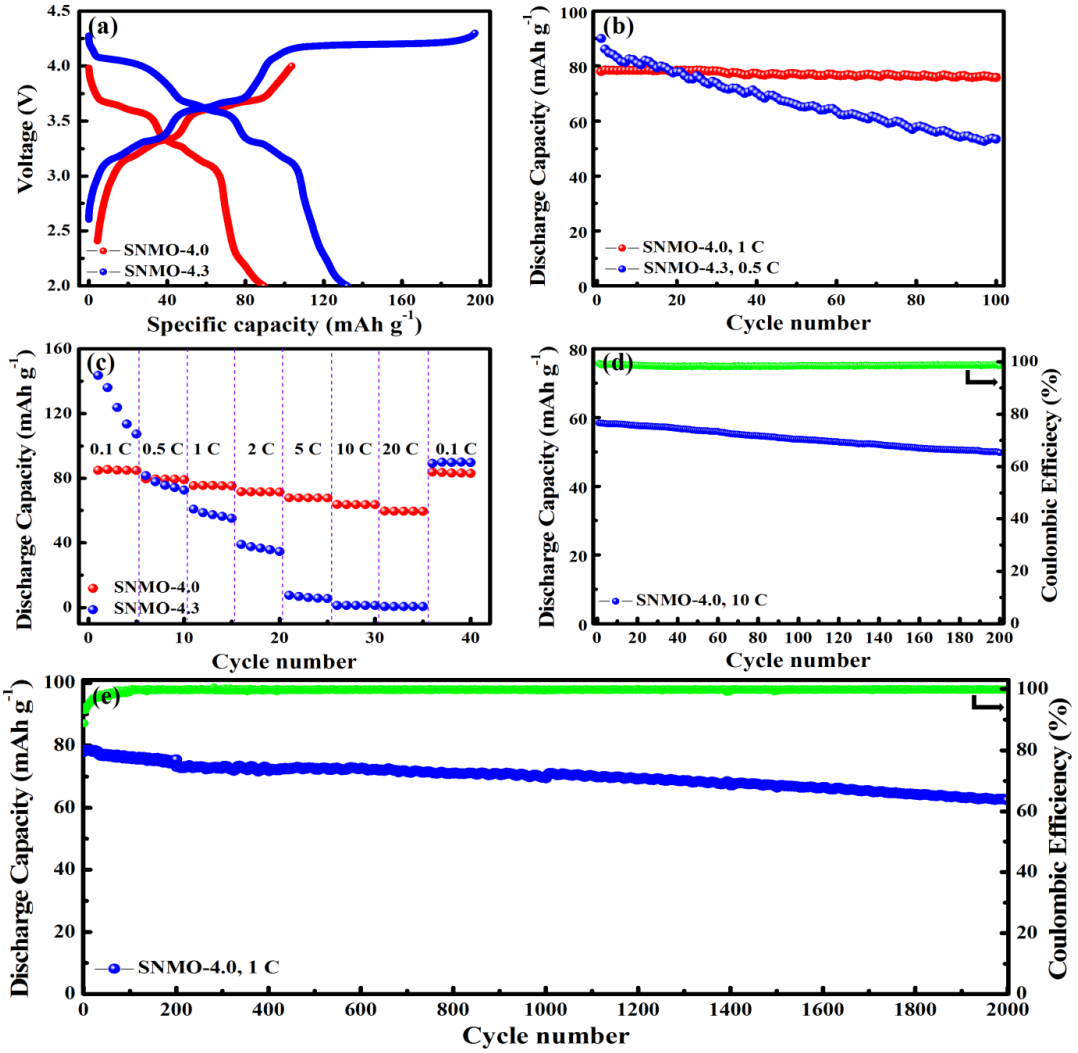
(a)
Voltage (V)
Specific capacity (mAh g-1)
SNMO-4.0
SNMO-4.3
(b)
Discharge Capacity (mAh g-1)
Cycle number
SNMO-4.0, 1 C
SNMO-4.3, 0.5 C
(c)
Discharge Capacity (mAh g-1)
Cycle number
0.1 C
0.5 C
1 C
2 C
5 C
10 C
20 C
0.1 C
SNMO-4.0
SNMO-4.3
(d)
Discharge Capacity (mAh g-1)
Coulombic Efficiecy (%)
Cycle number
SNMO-4.0, 10 C
(e)
Discharge Capacity (mAh g-1)
Coulombic Efficiency (%)
Cycle number
SNMO-4.0, 1 C

Figure 4

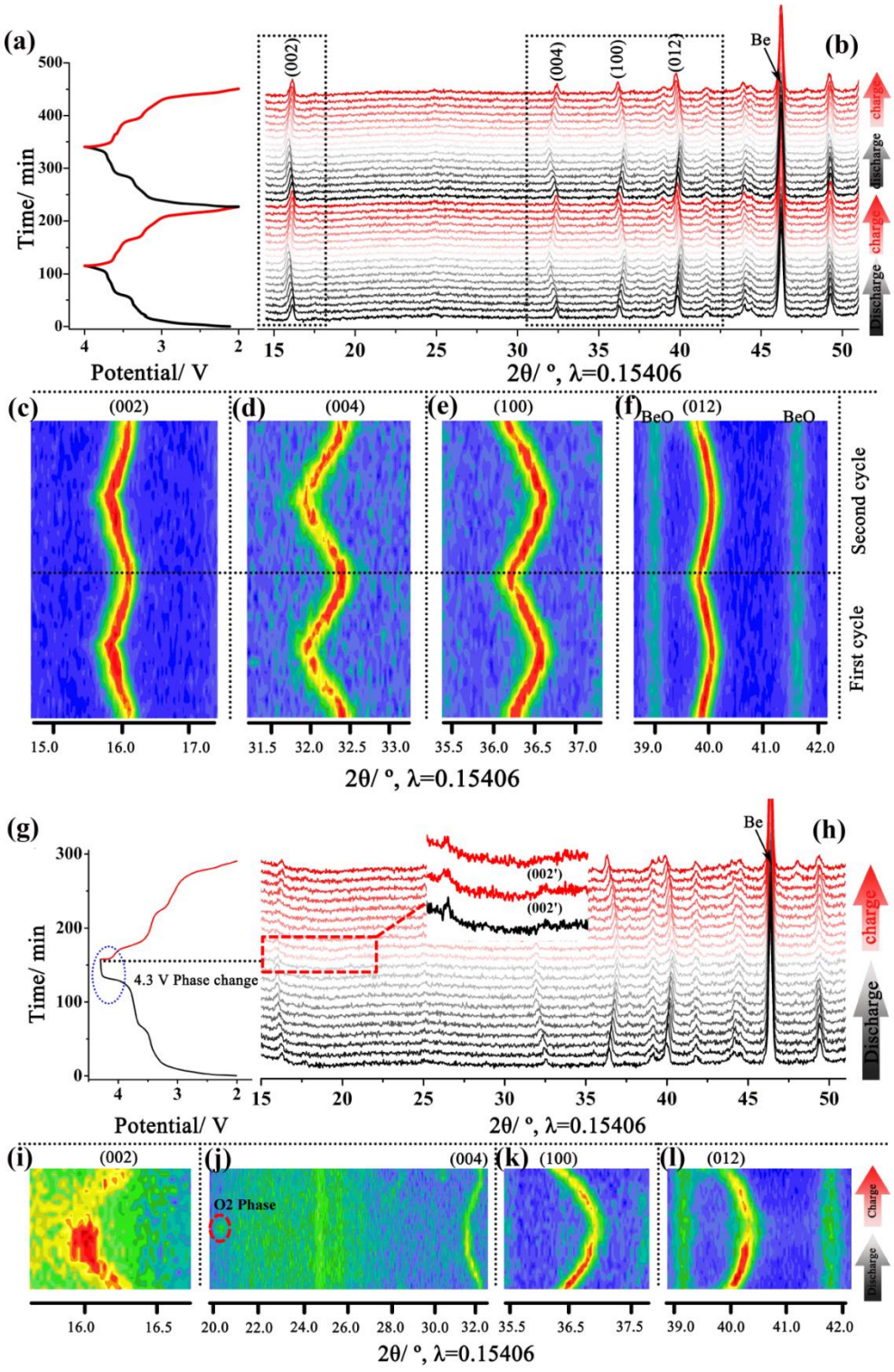
(a)
(b)
(002)
(004)
(100)
(012)
Be
Time/ min
Potential/ V
2θ/ °, λ=0.15406
charge
Discharge
(c)
(d)
(e)
(f)
BeO
Second cycle
First cycle
(g)
(h)
(002')
4.3 V Phase change
(i)
(j)
(k)
(l)
O2 Phase
Charge
Discharge

Figure 5

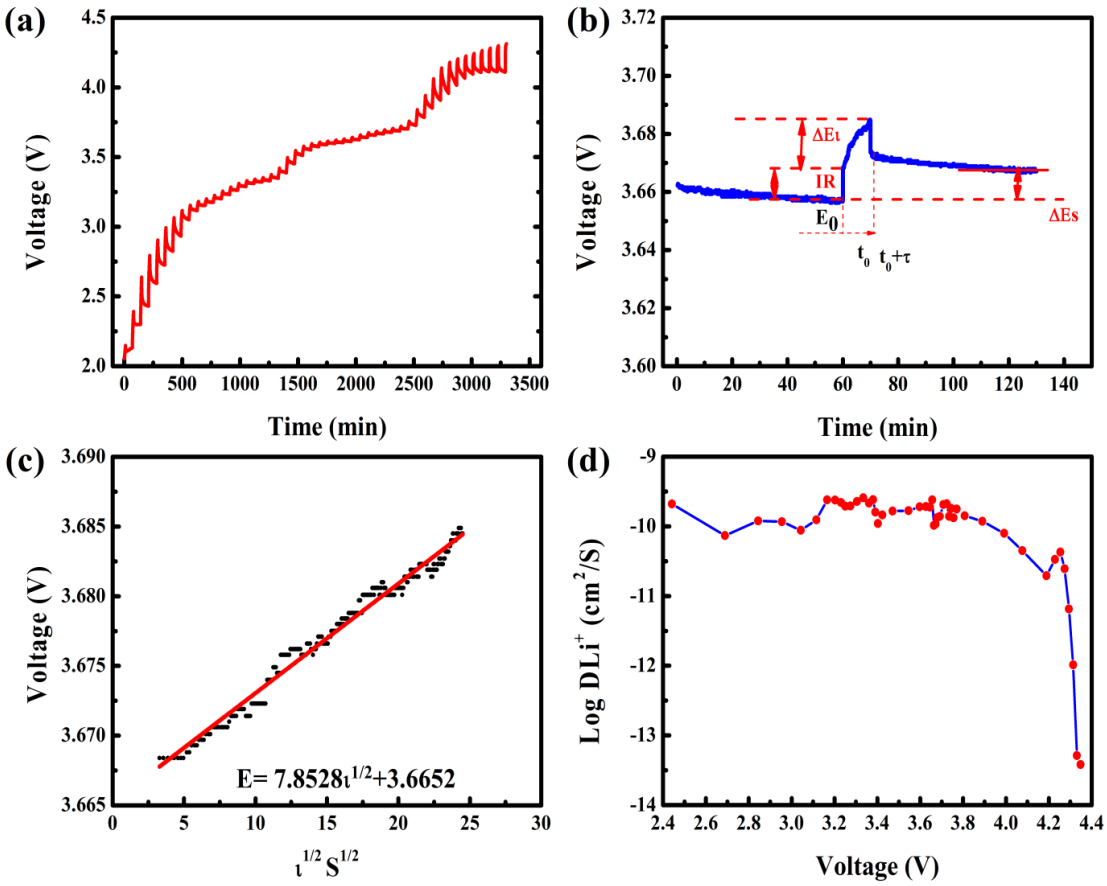
(a)
Voltage (V)
Time (min)
(b)
Voltage (V)
ΔEι
IR
E0
ΔEs
t0 t0+τ
Time (min)
(c)
Voltage (V)
E= 7.8528ι1/2+3.6652
ι1/2 S1/2
(d)
Log DLi+ (cm2/S)
Voltage (V)

Figure 6

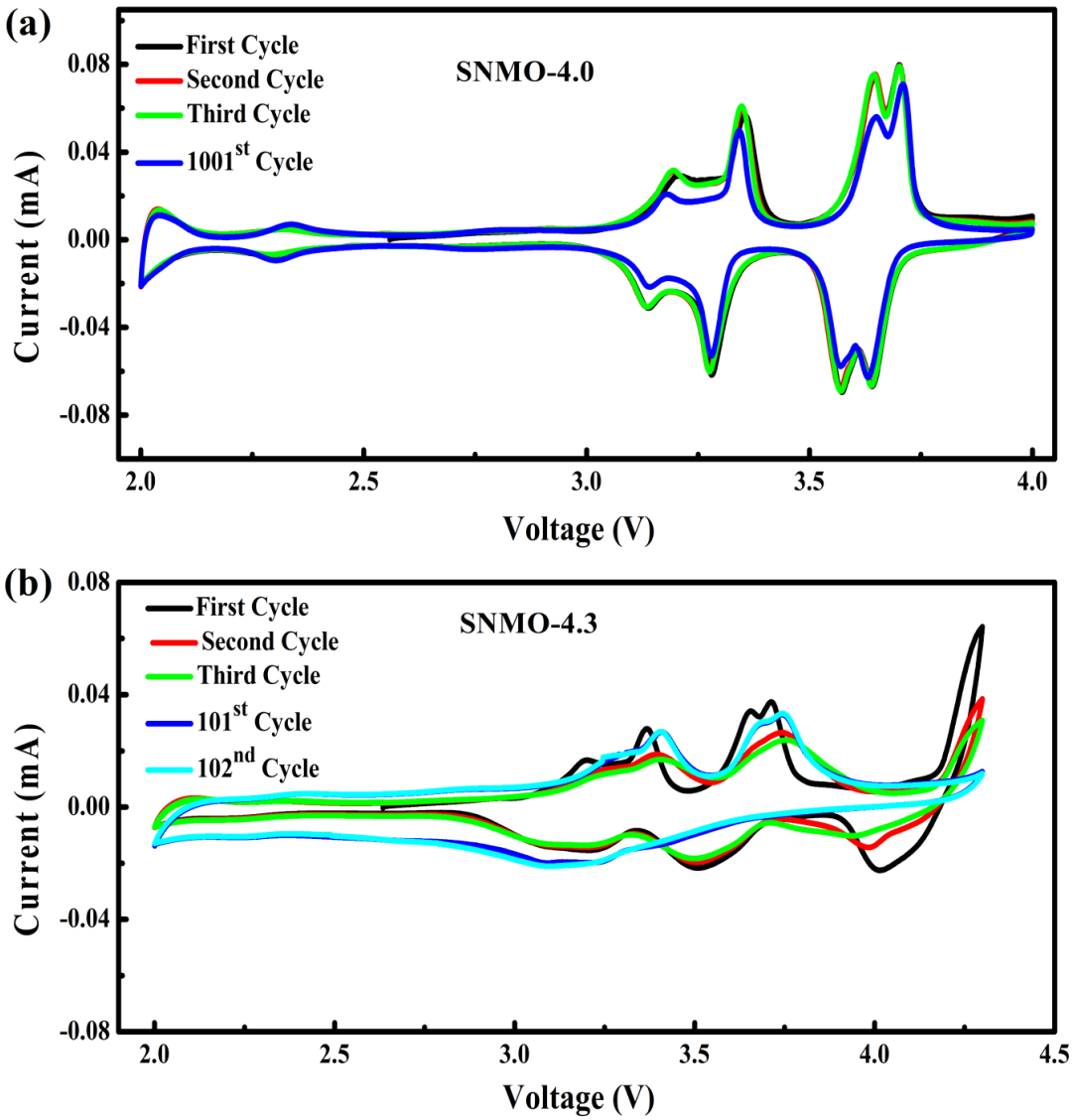
(a)
First Cycle
Second Cycle
Third Cycle
1001st Cycle
SNMO-4.0
Current (mA)
0.08
0.04
0.00
-0.04
-0.08
2.0
2.5
3.0
3.5
4.0
Voltage (V)
(b)
First Cycle
Second Cycle
Third Cycle
101st Cycle
102nd Cycle
SNMO-4.3
Current (mA)
0.08
0.04
0.00
-0.04
-0.08
2.0
2.5
3.0
3.5
4.0
4.5
Voltage (V)

Figure 7

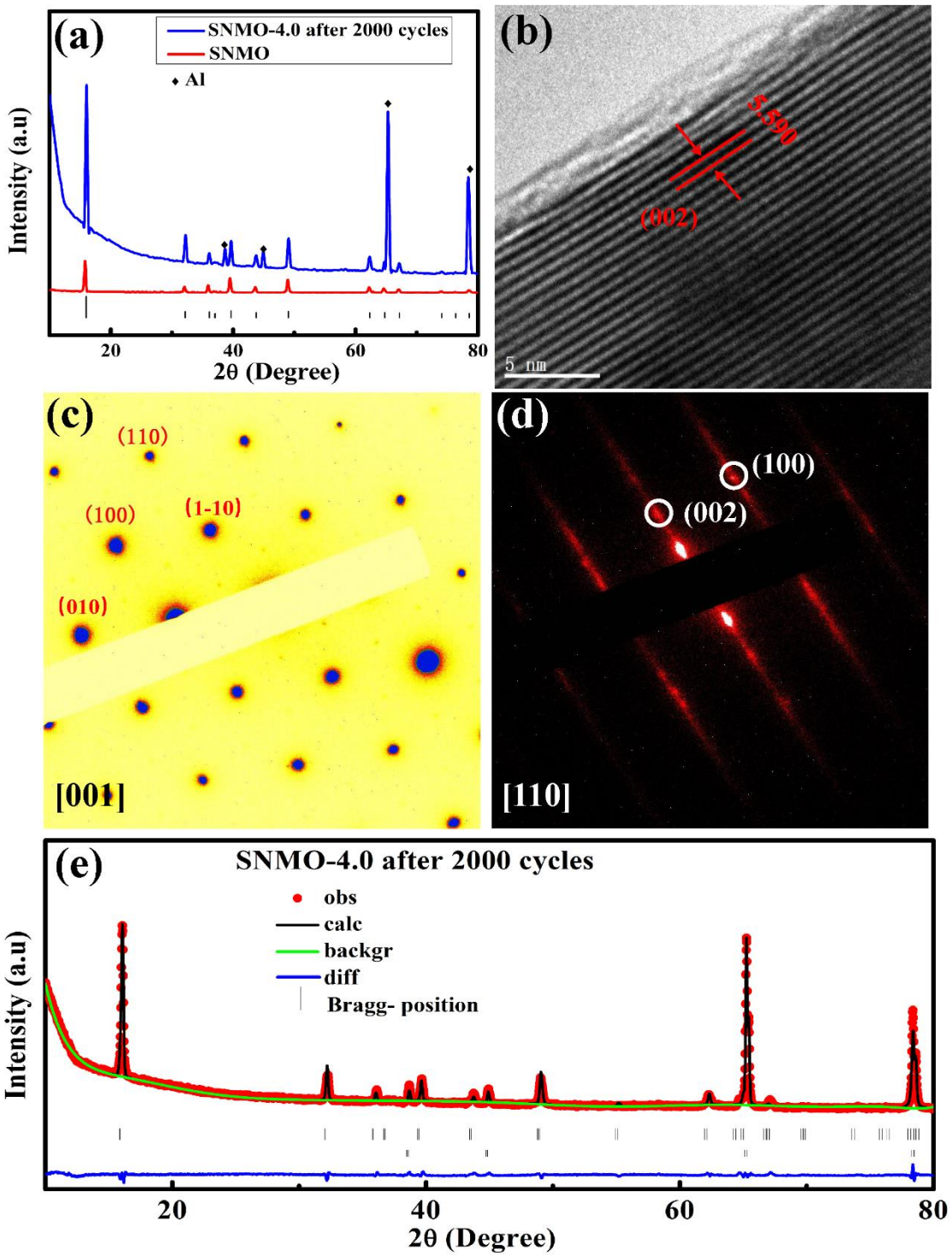
(a)
SNMO-4.0 after 2000 cycles
SNMO
Al
Intensity (a.u)
20
40
60
80
2θ (Degree)
(b)
5.590
(002)
5 nm
(c)
(110)
(100)
(1-10)
(010)
[001]
(d)
(100)
(002)
[110]
(e)
SNMO-4.0 after 2000 cycles
obs
calc
backgr
diff
Bragg- position
Intensity (a.u)
20
40
60
80
2θ (Degree)